

# Rotational velocities of Blue Straggler Stars in the Globular Cluster M55<sup>★</sup>

A. Billi<sup>1,2</sup>, F. R. Ferraro<sup>1,2</sup>, A. Mucciarelli<sup>1,2</sup>, B. Lanzoni<sup>1,2</sup>, M. Cadelano<sup>1,2</sup>, and L. Monaco<sup>3</sup>

<sup>1</sup> Dipartimento di Fisica e Astronomia, Università degli Studi di Bologna, Via Gobetti 93/2, I-40129 Bologna, Italy  
e-mail: alex.billi2@unibo.it

<sup>2</sup> INAF, Osservatorio di Astrofisica e Scienza dello Spazio di Bologna, Via Gobetti 93/3, I-40129 Bologna, Italy

<sup>3</sup> Universidad Andres Bello, Facultad de Ciencias Exactas, Departamento de Ciencias Físicas - Instituto de Astrofísica, Autopista Concepción-Talcahuano, 7100, Talcahuano, Chile

August 15, 2024

## ABSTRACT

By using high-resolution spectra acquired with FLAMES-GIRAFFE at the ESO/VLT, we measured radial and rotational velocities of 115 stars in the Galactic globular cluster M55. After field decontamination based on the radial velocity values, the final sample of member stars is composed of 32 blue straggler stars (BSSs) and 76 reference stars populating the red giant and horizontal branches of the cluster. In agreement with previous findings, the totality of red giant branch stars has negligible rotation ( $< 10 \text{ km s}^{-1}$ ), and horizontal branch stars have rotational velocities of  $40 \text{ km s}^{-1}$  at most. In contrast, the BSS rotational velocity distribution shows a long tail extending up to  $\sim 200 \text{ km s}^{-1}$ , with 15 BSSs (out of 32) spinning faster than  $40 \text{ km s}^{-1}$ . By defining the threshold for fast rotating BSSs at  $40 \text{ km s}^{-1}$ , this sets the percentage of these stars at  $47 \pm 14 \%$ . Such a large value has never been found before in any globular clusters. It is roughly comparable to that measured in other loose systems ( $\omega$  Centauri, M4, and NGC 3201) and significantly larger than that observed in high-density clusters (as 47 Tucanae, NGC 6397, NGC 6752, and M30). This evidence supports a scenario where recent BSS formation is occurring in low-density environments. We also find that the BSS rotational velocity tends to decrease for decreasing luminosity, as found for another loose cluster of the sample (namely, NGC 3201).

**Key words.** Blue Straggler Stars — Globular clusters — Spectroscopy — Rotational velocities

## 1. Introduction

Blue Straggler Stars (BSSs) are an “exotic” stellar population, not predicted by the standard stellar evolution theory. In the color-magnitude diagram (CMD) of Galactic globular clusters (GCs), they lie on a bluer (hotter) and brighter extension of the main sequence (MS; see, e.g., Ferraro et al. 1992, 1997, 2001, 2003), where stars more massive ( $M \sim 1.2\text{--}1.6 M_{\odot}$ ; Shara et al. 1997; Gilliland et al. 1998; De Marco et al. 2005; Fiorentino et al. 2014; Raso et al. 2019) than normal MS turnoff stars (with  $M \sim 0.8 M_{\odot}$ ) spend their core hydrogen-burning phase. Due to their large mass, BSSs are crucial gravitational test particles to probe internal dynamical processes occurring in GCs. Ferraro et al. 2012 proposed the concept of “dynamical clock”, a method based on the analysis of the BSS radial distribution to infer the level of dynamical evolution of star clusters. In this respect, the  $A_{rh}^+$  parameter (Alessandrini et al. 2016; Lanzoni et al. 2016) measures the degree of BSS central segregation with respect to a lighter reference population (typically red giant branch or MS stars) adopted as reference. This parameter has been found to efficiently trace the level of dynamical evolution experienced by star clusters (Ferraro et al. 2018, 2019, 2020, 2023a).

Two main scenarios for BSS formation have been suggested so far: mass transfer (MT) activity in binary systems (McCrea 1964), where the companion star transfers mass and angular momentum to the accreting proto-BSS that then becomes a MT-BSS, and direct collisions between two or more stars, produc-

ing collisional BSSs (COL-BSSs; Hills & Day 1976). The frequency of both formation channels can in principle be increased by mergers/collisions produced by the evolution of triple systems (Andronov et al. 2006; Perets & Fabrycky 2009). To shed light on the formation and the evolutionary processes of this class of exotica, several studies have been carried out in both open and globular clusters searching for evidence of the two formation channels and possible links between the observational properties of BSSs and those of the host parent cluster (e.g., Ferraro et al. 1993, 1995; Davies et al. 2004; Piotto et al. 2004; Sollima et al. 2008; Mathieu & Geller 2009; Geller & Mathieu 2011; Gosnell et al. 2014; Leigh et al. 2007, 2013).

Since MT-BSSs are produced by binary systems, this formation channel should be favored in low-density environments because, in conditions of high stellar crowding, binary systems are subject to multiple dynamical interactions that can disrupt them. Indeed, promising evidence of MT-BSSs has been found from both photometric and spectroscopic studies in low-density environments, such as loose GCs and open clusters. By analyzing *Hubble* Space Telescope (HST) photometric data of a sample of loose Galactic GCs, Sollima et al. 2008 found a positive correlation between the fraction of binary systems and that of BSSs, in agreement with what expected if MT activity in binaries is the main BSS formation channel. Moreover, an ultraviolet excess has been detected (Gosnell et al. 2014, 2015) in a few BSSs in the open cluster NGC 188, a stellar system with a very large fraction of BSSs in binary systems (Mathieu & Geller 2009). This has been interpreted as the evidence of the presence of a hot white dwarf (the remnant core of the original donor star at the

<sup>★</sup> Based on observations collected at the European Southern Observatory, Cerro Paranal (Chile), under Program 093.D-0270 (PI: Lovisi).

end of the MT phase), orbiting a newly formed BSS. From the chemical point of view, MT-BSSs are predicted to show anomalous surface abundances of carbon, nitrogen and oxygen, due to material partially processed by the CNO burning cycle in the innermost layers of the donor star, that is now accumulated onto the BSS surface (Sarna & De Greve 1996). Conversely, COL-BSSs are expected to show normal chemical abundances (Lombardi et al. 1995). A sub-sample of BSSs with carbon and oxygen depletion (the expected MT formation signature) has been indeed found both in 47 Tucanae (Ferraro et al. 2006) and in M30 (Lovisi et al. 2013b). Similarly, an enhancement in barium (Milliman et al. 2015, Nine et al. 2024) has been found in a few BSS in open clusters and interpreted as a signature of mass transfer from an asymptotic giant branch companion onto a proto-BSS.

A potential manifestation of COL-BSS comes from the photometric investigation of post-core collapse GCs. In fact, during the core collapse phase, the central density increases significantly, and this can trigger an enhancement of the collisional activity that contributes to the formation of COL-BSSs. Thus, the presence of a relatively new and coeval population of COL-BSSs with different masses is expected to be observable in stellar systems that experienced core collapse in their recent past. In accordance with this, the narrow blue sequence of BSSs, which appears to be well separated from a redder BSS sequence in the CMD of a few post-core collapse GCs (namely M30, NGC 362, M15 and NGC 6256; see Ferraro et al. 2009; Dalessandro et al. 2013; Beccari et al. 2019; Cadelano et al. 2022) has been interpreted as due to a population of COL-BSSs recently formed during the core collapse event.

The rotational velocity, instead, seems to not allow distinguishing between MT- and COL-BSSs. In fact, large rotational velocities are expected at birth for BSSs formed by both the channels, due to the transfer of mass and angular momentum for MT-BSSs (Packet 1981; Sarna & De Greve 1996; de Mink et al. 2013), and to the conservation of angular momentum for COL-BSSs (Benz & Hills 1987; Sills et al. 2002). However, braking mechanisms (such as magnetic braking and disk locking) are predicted to slow down the rotation of these stars as function of time (Leonard & Livio 1995; Sills et al. 2005; Leiner et al. 2018, Sun et al. 2024). The characteristic timescales of these processes are still largely unknown, and any new observational constraint is precious in this respect. Thus, although the rotational velocity cannot be used as a diagnostic of the formation mechanism, it could be an indicator of the BSS age (i.e., the amount of time passed from the end of MT, or from the collision that originated the BSS), and provide new physical information for a proper modeling of these objects.

In this context, several years ago our group started an high-resolution spectroscopic survey aimed at the chemical and kinematical characterization of BSSs belonging to GCs with different structural properties. Eight GCs have been observed so far: 47 Tucanae (Ferraro et al. 2006), NGC 6397 (Lovisi et al. 2012), NGC 6752 (Lovisi et al. 2013a), M30 (Lovisi et al. 2013b), M4 (Lovisi et al. 2010),  $\omega$  Centauri (Mucciarelli et al. 2014), NGC 3201 (Billi et al. 2023), and M55 (this paper). Using this dataset, Ferraro et al. 2023b found intriguing relations between the fraction of fast-rotating (FR) BSSs and the parent cluster structural parameters (such as central density and concentration), suggesting that rapidly spinning BSSs preferentially populate low-density environments. According to Ferraro et al. 2023b, FR-BSSs have been defined as those with projected rotational velocity  $v \sin(i) \geq 40 \text{ km s}^{-1}$ , with  $i$  being the inclination angle on the plane of the sky. In that paper, we analyzed the overall distribution of rotational velocities in a sample of 300 BSSs in 8

clusters, finding that it shows a significant drop at values larger than 30-50 km/s, thus suggesting an appropriate threshold value of 40 km/s. We also showed that the assumption of a slightly different threshold value does not affect the results. Among the investigated clusters, M55 is the one with the lowest values of central density ( $\log \rho_0 = 2.2$  in units of  $L_\odot \text{ pc}^{-3}$ ) and concentration parameter ( $c = 0.93$ ). This paper is devoted to the detailed presentation and discussion of the results obtained for the BSSs and the reference horizontal branch (HB) and red giant branch (RGB) stars observed in M55. We organized the paper in the following sections: the observations and data reduction are discussed in Section 2; the radial velocities measures and the determination of the atmospheric parameters for the cluster member stars are described in Sections 3 and 4, respectively; the determination of rotational velocities is presented in 5; Section 6 describes the obtained results and our conclusions.

## 2. Observations

This work is based on high resolution stellar spectra acquired with the multi-object spectrograph FLAMES-GIRAFFE (Pasquini et al. 2002) mounted at the Very Large Telescope of European Southern Observatory (ESO) under program 093.D-0270 (PI: Lovisi). All spectra have been acquired with the HR2 grating, with a spectral resolution  $R = 22,700$  in the wavelength range  $\Delta\lambda = 3854 - 4049 \text{ \AA}$ , in order to sample the Ca II K line at wavelength  $\lambda = 3933.663 \text{ \AA}$  that is very sensitive to the rotation of stars at high temperature (BSS and HB). For RGBs we used different lines of Fe and Ti. A total of 16 exposures of 2760 seconds each have been secured. The observations have been performed in 9 nights between June and July 2014. Six exposures had bad sky conditions (moon distance and airmass) so we excluded them from the analysis. The spectra have been acquired for 115 targets selected along the HB, the RGB, and the BSS sequence in the UV and optical CMDs presented in Lanzoni et al. 2007. The standard pre-reduction steps (bias subtraction, flat field correction, wavelength calibration, and the one-dimensional spectra extraction) have been performed using the dedicated ESO pipeline<sup>1</sup>. The sky contribution has been subtracted from the observed spectra by using a master-sky spectrum obtained as the median of all the sky spectra of each exposure. Then, the sky-subtracted and heliocentric velocity-corrected spectra of each target have been combined together. The S/N ratio for the BSS sample ranges between 15 and 30. Instead, the S/N ratio for HBs and RGBs ranges between 25 - 70 and 15 - 70 respectively.

## 3. Radial velocities and cluster membership

The radial velocities ( $V_r$ ) of the sampled stars have been measured by using the IRAF task *fxcor* that performs a cross-correlation between the observed spectrum and a template spectrum of known  $V_r$  (Tonry & Davis 1979). As templates we adopted synthetic spectra computed with the code SYNTHE (Sbordone et al. 2004; Kurucz 2005) for BSSs, HB and RGB stars, to take into account their different stellar parameters and the different line strengths. The last version of the Kurucz/Castelli linelist for atomic and molecular transitions has been adopted. We calculated the model atmospheres for the synthetic spectra with the ATLAS9 code (Kurucz 1993; Sbordone et al. 2004) under the assumptions of local thermodynamic equilibrium (LTE) and plane-parallel geometry, and adopting the

<sup>1</sup> <http://www.eso.org/sci/software/pipelines/>

**Table 1.** Properties of the analyzed BSSs.

ID	R.A. [deg]	Decl. [deg]	B	(B-I)	$V_R$ [km s $^{-1}$ ]	$v \sin(i)$ [km s $^{-1}$ ]	Var
100108	294.9850000	-30.9720000	15.99	0.29	$178.3 \pm 0.2$	$> 200$	
100101	294.9927917	-30.9853056	16.21	1.04	$178.1 \pm 1.6$	$21 \pm 3$	SXP
2700607	295.0269583	-30.9911389	16.25	0.68	$177.5 \pm 8.5$	$107 \pm 15$	SXP
200142	295.0122083	-30.9582222	16.35	0.66	$179.3 \pm 1.9$	$95 \pm 6$	SXP
2700663	294.9460417	-30.9597222	16.54	0.98	$174.8 \pm 1.9$	$20 \pm 4$	SXP
2700733	295.0367500	-30.9546111	16.59	0.60	$147.8 \pm 12.0$	$202 \pm 15$	SXP
2800072	295.0967083	-30.9473611	16.59	0.96	$173.6 \pm 1.3$	$125 \pm 4$	
2700739	294.9941667	-30.9064444	16.63	0.68	$169.4 \pm 4.9$	$69 \pm 4$	
2700785	294.9553750	-30.9422222	16.73	0.77	$163.3 \pm 0.1$	$68 \pm 5$	SXP
2700747	294.9772917	-30.9997222	16.76	0.83	$174.5 \pm 6.7$	$70 \pm 4$	SXP
2700813	295.0688333	-30.9846944	16.79	0.64	$186.7 \pm 2.9$	$39 \pm 3$	
2700834	295.0217500	-30.9895556	16.84	0.59	$182.1 \pm 8.9$	$104 \pm 10$	EW
200178	295.0122917	-30.9748333	16.85	0.74	$179.6 \pm 1.6$	$17 \pm 2$	SXP
200196	294.9982500	-30.9483611	16.89	0.60	$176.8 \pm 1.3$	$225 \pm 15$	SXP
200204	295.0167500	-30.9705278	16.91	0.77	$173.4 \pm 4.5$	$199 \pm 15$	SXP
2700918	294.9522917	-30.9461389	17.03	0.72	$173.0 \pm 1.1$	$62 \pm 10$	SXP
2700925	294.9459583	-30.8815278	17.03	0.67	$179.3 \pm 1.4$	$17 \pm 3$	
100215	294.9859583	-30.9600833	17.05	0.50	$182.0 \pm 6.2$	$19 \pm 2$	
2701036	295.0175000	-30.9150278	17.23	0.89	$176.6 \pm 1.4$	$37 \pm 2$	
200256	295.0286250	-30.9425556	17.32	0.78	$177.8 \pm 1.2$	$12 \pm 2$	SXP
2701130	295.0383333	-30.9453056	17.32	0.89	$167.5 \pm 0.7$	$9 \pm 3$	SXP
100252	294.9789583	-30.9728611	17.35	0.34	$176.1 \pm 3.6$	$4 \pm 1$	SXP
2701162	294.9395000	-30.9343611	17.39	0.79	$175.7 \pm 4.0$	$40 \pm 4$	SXP
2701145	294.9740000	-31.0132222	17.39	0.81	$172.5 \pm 1.2$	$< 3$	SXP
100256	294.9752083	-30.9690278	17.46	0.81	$180.3 \pm 5.6$	$35 \pm 4$	SXP
100280	294.9942083	-30.9569444	17.47	0.67	$174.3 \pm 3.5$	$< 3$	SXP
2701235	295.0499583	-31.0348889	17.50	0.72	$174.2 \pm 3.4$	$26 \pm 3$	SXP
2701308	295.0078750	-30.9275556	17.53	0.76	$171.3 \pm 4.1$	$69 \pm 6$	SXP
2701374	294.9658750	-30.9316389	17.57	0.81	$189.3 \pm 1.1$	$< 3$	SXP
2701376	295.0330417	-30.9474167	17.63	0.93	$189.1 \pm 1.4$	$59 \pm 4$	SXP
200354	295.0214583	-30.9805278	17.68	0.88	$174.2 \pm 1.4$	$20 \pm 4$	
2701676	294.9928333	-30.9187778	17.92	1.08	$171.2 \pm 1.6$	$< 3$	

**Notes.** Identification number, coordinates, B-band magnitude and (B-I) color (from Stetson et al. 2019), radial velocity, rotational velocity, and variability type of the analyzed BSSs. The variability is from Kaluzny et al. 2010: SXP means SX Phoenicis, while EW is for contact binary. #100108 does not have the  $v \sin(i)$  error because the estimated  $v \sin(i)$  is a lower limit.

opacity distribution functions by Castelli & Kurucz 2003 with no inclusion of the approximate overshooting prescription (Castelli et al. 1997).

Figure 1 shows the distribution of the measured  $V_r$  of the 115 targets as a function of the distance from the cluster center. The vast majority of the targets defines a narrow distribution strongly peaked at the systemic velocity of the cluster. The mean value and the standard deviation of the mean obtained from our sample turn out to be  $175.1 \pm 0.5$  km s $^{-1}$ , while the standard deviation of the sample is  $\sigma = 5.2$  km s $^{-1}$ , and nicely agrees with the systemic velocity quoted in Baumgardt & Hilker 2018 ( $< V_r > = 174.8 \pm 0.2$  km s $^{-1}$ ). Such a narrow distribution allows a straightforward identification of the few field stars contaminating the observed sample: indeed only 7 targets (corresponding to 6% of the total sample) display much smaller radial velocities (well below  $< V_r > = 50$  km s $^{-1}$ ) and can thus be safely considered as field interlopers (gray circles in Fig. 1). Thus, we considered as member stars those within  $3\sigma$  from the cluster systemic velocity. Only one star (namely #2700733) is marginally consistent with this assumption within the errors. This is a fast rotator and for this reason the measure of its radial velocity turns out to be more uncertain than the others (see Table 1). However (as

shown in Figure 1) the mean radial velocity of field stars in this region of the sky ( $< V_r > = -23.1 \pm 18.5$  km s $^{-1}$ ) is very different from that of the cluster ( $< V_r > = 175$  km s $^{-1}$ ). Hence, the probability that this star is a field interloper is very low. Moreover, its proper motion (from Gaia DR3) turns out to be fully consistent with that of the cluster, thus further confirming its membership. In summary, our sample of likely cluster members include 32 BSSs, 30 RGB and 46 HB stars. The 32 surveyed BSSs are a representative sub-sample of the entire population, which in this cluster counts 55-58 objects. In addition, they have been selected to secure adequate sampling of both the luminosity extension of the BSS sequence, and the BSS radial distribution. Also the HB sample can be considered representative, since it covers the entire distribution in color (temperature) of the HB evolutionary stage. On the other hand, the few observed RGB stars are just meant to provide a reference population of slow rotators. The most relevant criterium adopted for the target selection is to avoid contamination of the spectra from scattered light from close neighbors. Hence, all the potential targets having stars of comparable or brighter luminosity within a distance of about 3" (which is more than twice the spectroscopic fiber size) have been excluded from the selection.

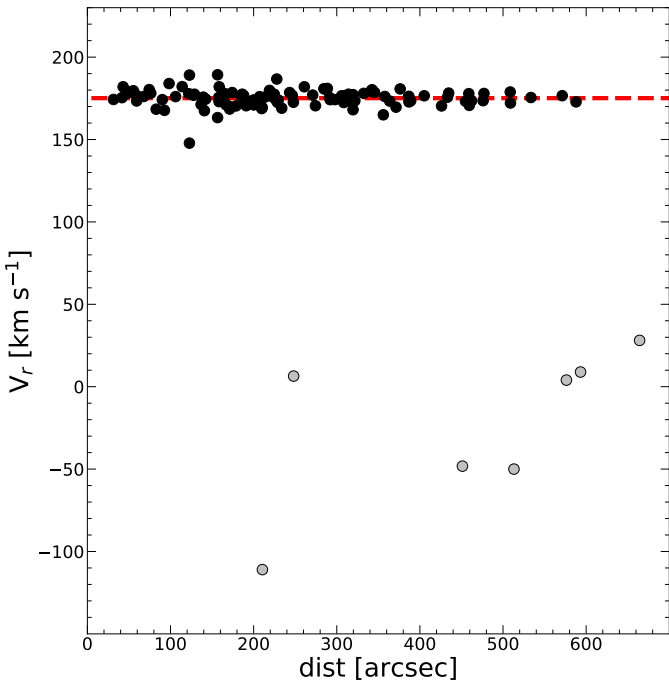


**Fig. 1.** Radial velocity distribution, as a function of the distance from the cluster center, obtained from the acquired spectra. The black and gray circles correspond to cluster members and Galactic field interlopers, respectively. The red dashed line marks the average radial velocity of the member star sample.

For the sake of illustration, Figure 2 shows their position in the (B, B-I) CMD obtained from ground-based photometry (Stetson et al. 2019).

#### 4. Atmospheric parameters

The values of effective temperature ( $T_{\text{eff}}$ ) and surface gravity ( $\log g$ ) of the spectroscopic targets, have been estimated from the comparison of their positions in the CMD with reference theoretical models. We used isochrones and HB models from the BASTI-IAC database (Pietrinferni et al. 2021), adopting an  $\alpha$ -enhanced mixture and a metallicity  $[\text{Fe}/\text{H}] = -1.94$  dex (Harris 1996). To transform the models into the observational CMD, we adopted the distance modulus quoted in Harris 1996 and then applied a slightly larger value of the reddening,  $E(\text{B}-\text{V}) = 0.11$  mag instead of  $E(\text{B}-\text{V}) = 0.08$  (as quoted in Harris 1996), to optimize the match between the models and the data. We used an HB model with masses ranging from  $0.5 M_{\odot}$  to  $0.75 M_{\odot}$ , a 13 Gyr-old isochrone (according to the age estimate by VandenBerg et al. 2013; note that adopting a slightly younger age has a negligible impact on the temperature and gravity determination) well reproducing the RGB location, and a set of isochrones with ages ranging from 2 Gyr to 9 Gyr that properly sample the BSS region of the CMD (see solid lines in Fig. 2). Each spectroscopic target has been orthogonally projected on the closest model, and the corresponding temperature and gravity have been associated. The resulting values of  $T_{\text{eff}}$  and  $\log g$  range between 7500-13400 K and 3.0-4.1 dex, respectively, for the HB stars, while for the RGB targets we find  $\Delta T_{\text{eff}} = 4800-5400$  K and  $\Delta \log g = 1.7-3.3$  dex, and for the surveyed BSS sample we obtain  $\Delta T_{\text{eff}} = 6800-9700$  K and  $\Delta \log g = 3.6-4.3$  dex. Finally, a microturbulence of  $1 \text{ km s}^{-1}$  has been assumed for BSSs and HB stars, while  $1.5 \text{ km s}^{-1}$  has been used for the RGB sample, which are typical values for stars with such temperatures and surface gravities. Note that

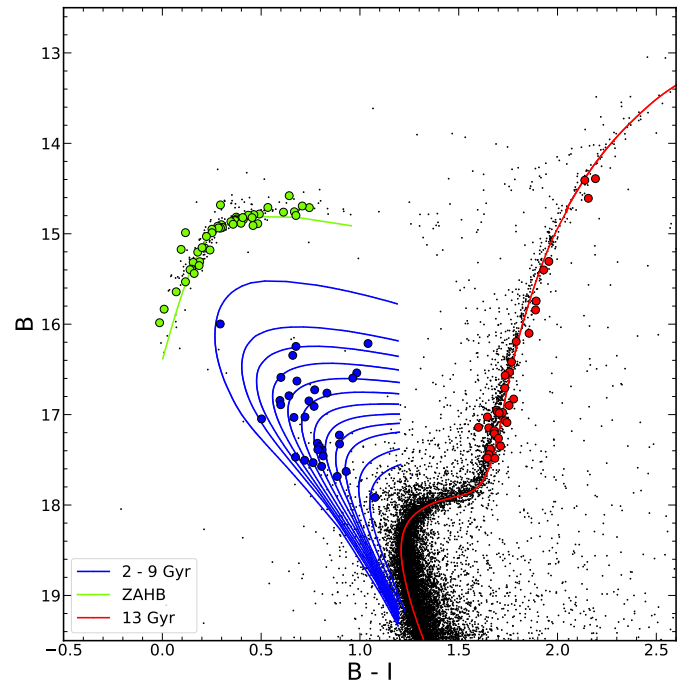


**Fig. 2.** CMD of M55 (black dots) with the surveyed BSS, RGB and HB stars marked, respectively, as blue, red, and green circles. A set of BASTI isochrones (Pietrinferni et al. 2021) with ages ranging from 2 to 9 Gyr are overplotted as blue lines, a BASTI isochrone of 13 Gyr is overplotted as red line, and a BASTI HB model is overplotted as green line.

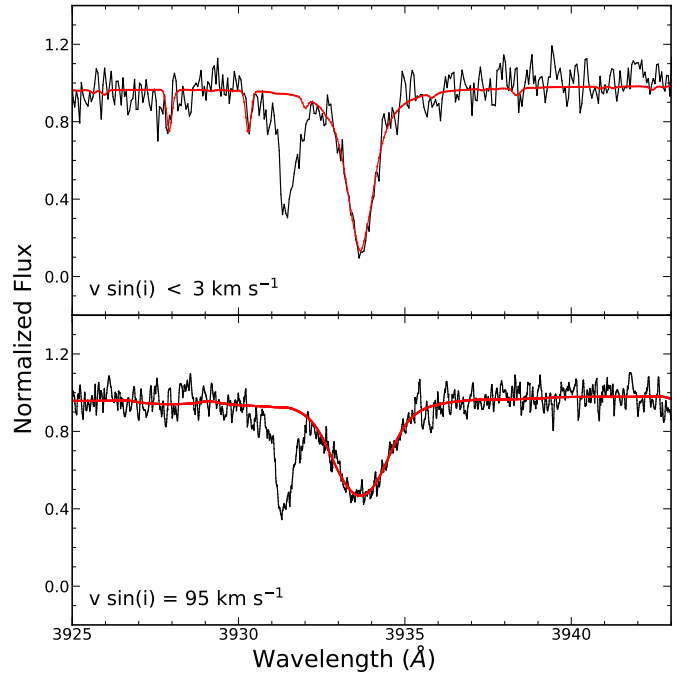


**Fig. 3.** Comparison between the observed spectra (black lines) and the synthetic spectra (red lines) of two BSSs with different rotational velocities (see labels).

varying this parameter has a negligible impact on the derived rotational velocities.

## 5. Rotational velocities

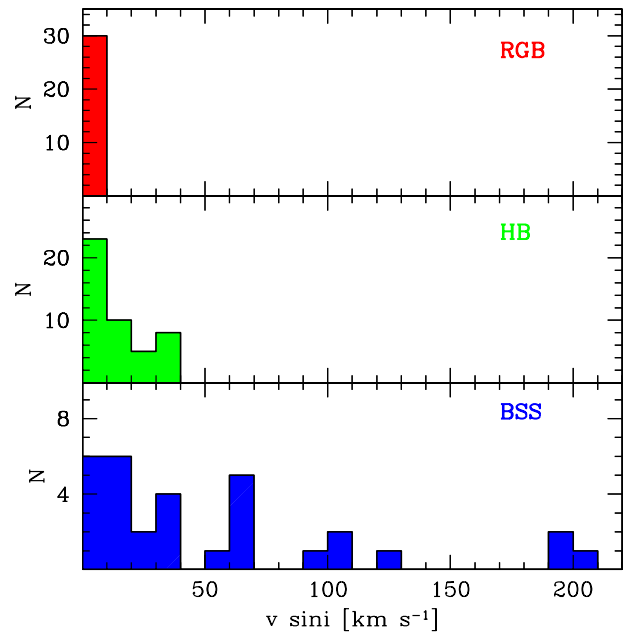
The rotational velocities projected on the line of sight ( $v \sin(i)$ ) have been determined from the comparison between each observed spectrum and a grid of synthetic spectra computed with the atmospheric parameters appropriate for the star under consideration, and different rotational velocities; a  $\chi^2$  minimization procedure then finds the most appropriate value of  $v \sin(i)$  needed to reproduce the observations. This has been done in the spectral region around the Ca II K absorption line at  $\lambda = 3933.663\text{\AA}$ . For the sake of illustration, Figure 3 shows the comparison between the observed and the synthetic spectra of two BSSs with different rotational velocities. As can be appreciated, a large value of  $v \sin(i)$  causes a large broadening of the line width.<sup>2</sup> For very slowly rotating BSSs we assume an upper limit of  $3 \text{ km s}^{-1}$  for their  $v \sin(i)$  value, because this is the typical uncertainty obtained from the Monte Carlo simulations for these objects.

The uncertainties in the rotational velocities obtained with this procedure have been estimated by using Monte Carlo simulations: a simulated spectrum with the same signal-to-noise ratio of the observed one has been obtained by randomly adding poissonian noise to the best-fitting synthetic template, and its rotational velocity has been determined with the same procedure applied to the data; after 300 realizations of such realistic simulated spectra, the standard deviation of the derived  $v \sin(i)$  distribution has been adopted as  $1\sigma$  uncertainty in the rotational velocity of each star. The estimated uncertainties range from a few (2-5)  $\text{km s}^{-1}$  for slowly rotating stars, up to 10-15  $\text{km s}^{-1}$  for the fast-spinning targets.

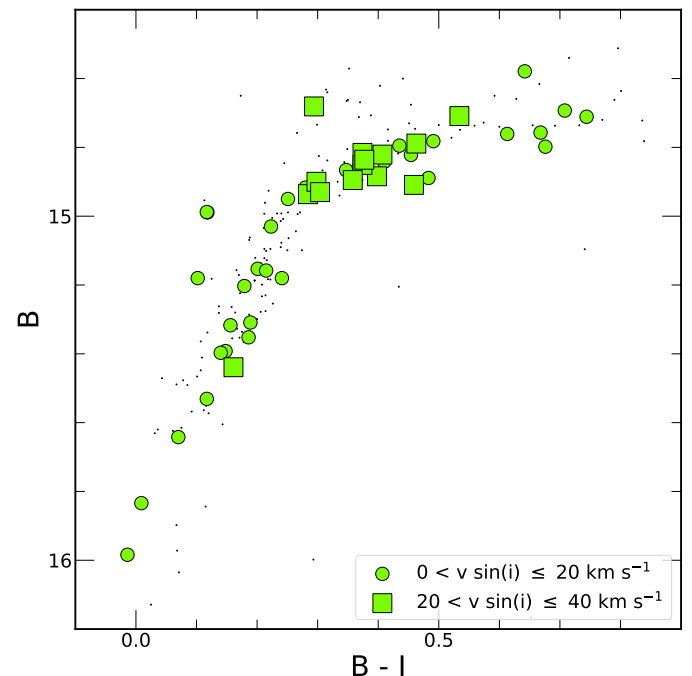
Figure 4 shows the comparison of the rotational velocity distributions obtained for the reference populations (RGB and HB stars) and the BSS sample. All RGB stars are consistent with null or very slow rotation ( $v \sin(i) < 10 \text{ km s}^{-1}$ ), while the HB targets show intermediate rotational velocity values, always smaller than  $40 \text{ km s}^{-1}$ . The distribution found for BSSs, instead, is much broader, with a tail extending up to rotational velocities of  $\sim 200 \text{ km s}^{-1}$ . Assuming the same definition of FR stars provided by Ferraro et al. 2023b (namely, stars with rotational velocity  $\geq 40 \text{ km s}^{-1}$ ), we conclude that the fraction of FR objects is zero in both the reference (RGB and HB) samples, while it rises to  $\sim 47 \pm 14\%$  (15/32) for the BSS population. This is the largest fraction of FR BSSs ever detected in a GC. This result will be discussed in Section 6.

Figure 5 shows a zoom in the HB region of the CMD, with different markers corresponding to stars spinning faster and slower than  $20 \text{ km s}^{-1}$  (see the legend). With the exception of just one object (out of 13), the HB stars showing large  $v \sin(i)$  are located in the redder part of the sequence, at  $(B-I) > 0.2$ , while at bluer colors only slowly rotating HB stars are found. A decrease of  $v \sin(i)$  for increasing effective temperature in HB stars has been already observed in other GCs, for instance in M13, M15 and NGC 6397 (Behr et al. 2000b, Behr et al. 2000a, Lovisi et al. 2012), but the physical mechanism that reduces the rotation in hot HB stars is not fully understood yet. Sills & Pinsonneault 2000 suggested that this might be due to the onset of gravitational settling mechanisms. The strong gradient in the element

<sup>2</sup> The additional absorption line which is visible in the observed spectra at  $\lambda \sim 3931.3\text{\AA}$  is due to the interstellar medium along to the line of sight. Note that the wavelength of this feature readable from Figure 3 is not the rest frame one, because we shifted the observed stellar spectrum to the rest frame to make an appropriate comparison with the synthetic one, but the interstellar medium has a radial velocity different from that of M55.



**Fig. 4.** Rotational velocity distributions of RGB stars (top panel), HB stars (middle panel), and BSSs (bottom panel).



**Fig. 5.** HB region of the CMD of M55 with the observed stars highlighted with different markers: small green circles for HB stars with  $v \sin(i) \leq 20 \text{ km s}^{-1}$ , large green squares for those rotating faster (up to  $40 \text{ km s}^{-1}$ ).

abundances can suppress the angular momentum transport and this prevents the stars to have high  $v \sin(i)$ . Vink & Cassisi 2002 argued that the decrease in rotational velocity for HBs hotter than 11,000 K is due to a loss of angular momentum caused by stellar winds set up by the radiative levitation.

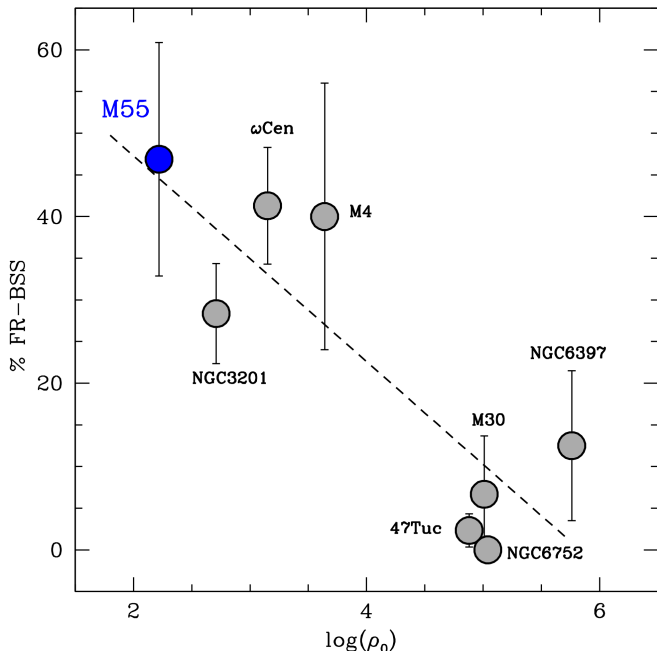
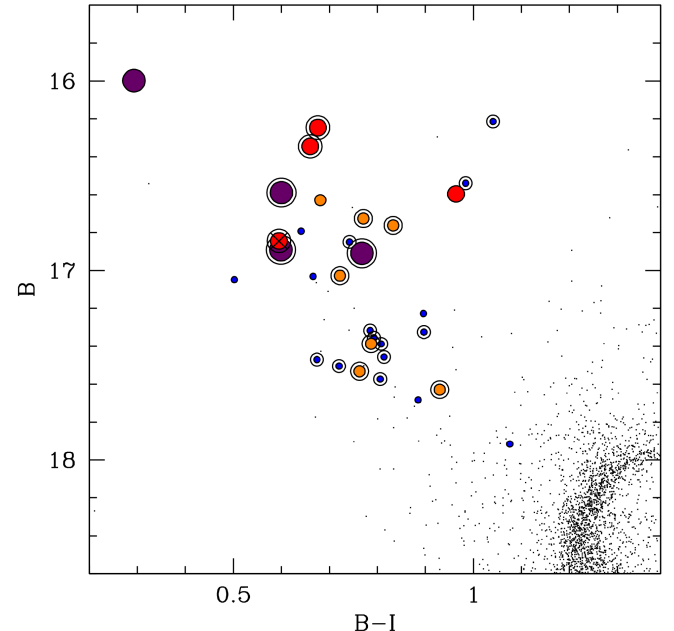


**Fig. 6.** Percentage of FR-BSSs as a function of the central density of the parent cluster, for the systems studied in Ferraro et al. 2023b. The position of M55 is highlighted in blue.

## 6. Discussion and conclusions

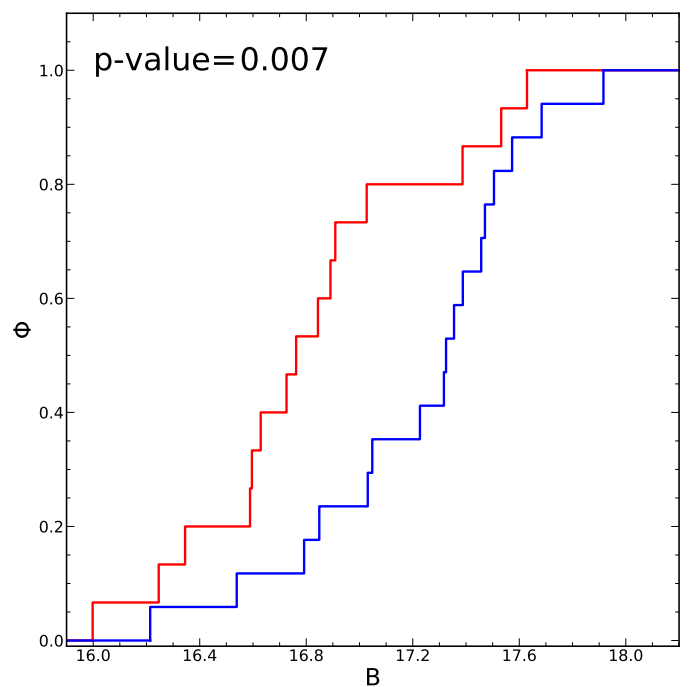
This work presents the results of a study about the rotational velocities of BSSs in the Galactic GC M55. As shown in Figure 4, while the reference (RGB and HB) stars are all slow rotators, with values of  $v \sin(i)$  below the threshold of  $40 \text{ km s}^{-1}$ , the BSS rotational velocity distribution shows a more complex distribution with a long tail extending at high values, up to  $\sim 200 \text{ km s}^{-1}$ . This distribution is similar to those found in M4 (Lovisi et al. 2010),  $\omega$  Centauri (Mucciarelli et al. 2014) and NGC 3201 (Billi et al. 2023). All these clusters are part of the sample studied in Ferraro et al. 2023b, where a significant anti-correlation has been found between the fraction of FR-BSSs and some structural and dynamical parameters of the parent cluster (such as the central density and the concentration parameter). In Figure 6 we report the behavior of the percentage of FR-BSSs as a function of the parent cluster central density, with M55 highlighted in blue. As can be seen, this is the system with the largest fraction of FR-BSSs and the smallest central density in the sample of GCs investigated so far.

Figure 7 shows the location of the measured BSSs in the CMD, plotted as circles of different sizes and colors depending on their rotational velocity: the slowly rotating BSSs (with  $v \sin(i) < 40 \text{ km s}^{-1}$ ) are plotted as small blue circles, while FR-BSSs are increasingly larger circles with orange color for  $v \sin(i)$  between 40 and  $80 \text{ km s}^{-1}$ , red color for rotational velocities ranging from 80 to  $180 \text{ km s}^{-1}$ , and violet color for the high-rotation tail, with  $v \sin(i) \geq 180 \text{ km s}^{-1}$ . We also checked our BSS sample for variability, performing a cross-correlation with the catalog of Kaluzny et al. 2010 and finding that 23 (out of 32) of the sampled BSSs are indeed variables (see large empty circles in Figure 7): 12 of them are FR-BSSs, while the remaining 11 are slow rotators. Almost all the detected variables (22 out of 23) are non binary systems, but pulsating stars classified as SX Phoenicis. The only exception star #2700834 (red cross in the figure), which is cataloged as a contact binary with asymmetric



**Fig. 7.** CMD of M55 zoomed in the BSS region, with the measured BSSs highlighted as large colored circles. The slowly rotating BSSs are marked with small blue circles. The FR-BSSs are plotted as increasingly larger circles for different rotational velocities (in units of  $\text{km s}^{-1}$ ): orange color for  $40 \leq v \sin(i) < 80$ , red color for  $80 \leq v \sin(i) < 180$ , and violet for  $v \sin(i) \geq 180 \text{ km s}^{-1}$ . All the BSSs identified as variable stars in the Kaluzny et al. 2010 catalog are highlighted with large open circles. The FR-BSS classified as contact binary is marked with a large black cross.

maxima as consequence of mass transfer. This is a FR-BSS with  $v \sin(i) = 104 \text{ km s}^{-1}$ , thus possibly indicating a system where MT is still ongoing, hence a proto-BSS in its way of formation.



**Fig. 8.** Cumulative distribution of FR-BSSs (red line) and slowly rotating BSSs (blue line) as a function of the B magnitude.

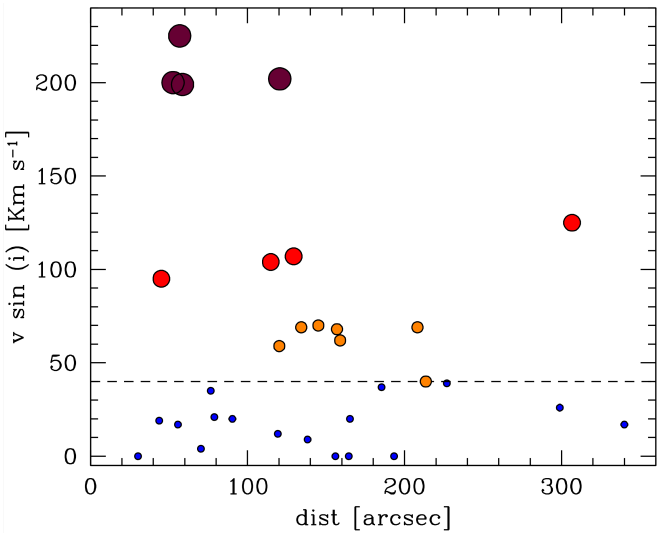


**Fig. 9.** BSS rotational velocities as a function of the radial distance from the cluster center. The symbols are as in Fig. 7. The dashed line marks the threshold adopted to distinguish fast-rotating from slowly rotating stars, namely  $v \sin(i) = 40 \text{ km s}^{-1}$ .

Indeed, a high rotational velocity is commonly interpreted as a signature of recent BSS formation activity (see Section 1), but braking mechanisms are expected to then intervene and slow down the stars (Leonard & Livio 1995; Sills et al. 2005). Although timescales and efficiencies of these mechanisms are not fully understood yet, some constraints are starting to emerge from observational studies. The analysis of BSS rotation in open clusters (Leiner et al. 2018) suggests a timescale of the order of 1 Gyr for products of the MT formation scenarios. On other hand, by combining considerations on the formation epoch of COL-BSSs in the post-core collapse cluster M30 (Ferraro et al. 2009; Portegies Zwart 2019) with the BSS rotation distribution presented in Lovisi et al. 2013a, a braking time-scale of 1-2 Gyr has been inferred also for COL-BSSs (Ferraro et al. 2023b). Thus, a large percentage of FR-BSSs reasonably traces a recent activity of BSS formation in the host cluster. The MT scenario should be dominant in low density environments, where stellar collisions are thought to be negligible. Hence, the correlation between the percentage of FR-BSSs and the binary fraction found in Ferraro et al. 2023b indicates that an high percentage of FR-BSSs in low density systems (Fig. 6) should be interpreted as the evidence of recent BSS formation activity due to the MT channel in primordial binaries.

The inspection of the Fig. 7 also suggests that FR-BSSs tend to populate the brightest portion of the BSS sequence: 12 FR-BSSs (out of 18 surveyed stars) are found at  $B < 17.2$ , while only 3 FR-BSSs (out of 14) can be counted in the lower portion of the sequence, thus indicating that FR-BSSs tend to be more luminous than slowly rotating BSSs. This is also supported by the cumulative magnitude distribution of the samples of slowly and rapidly rotating BSSs shown in Figure 8. By using a Kolmogorov-Smirnov test, we find that the probability that the two distributions are extracted from the same parent population is of the order of 0.7% (roughly corresponding to a  $2.5\sigma$  significance level). This is in good agreement with what observed in NGC 3201 (Billi et al. 2023). Conversely, we found no clear difference between the cumulative color (temperature) distributions of slow and fast rotating BSSs.

The dependence between rotational velocity and cluster-centric distance for the BSSs surveyed in M55 is plotted in Fig-

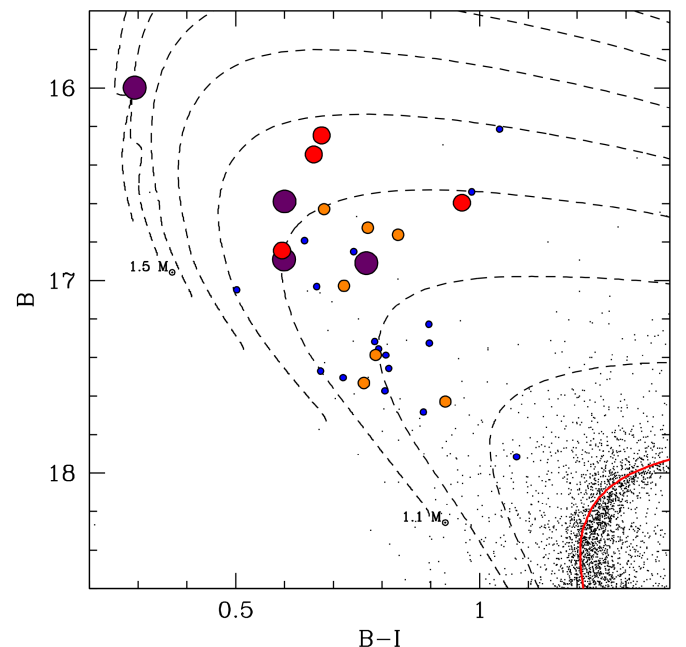


**Fig. 10.** CMD of M55 zoomed in the BSS region, with the surveyed BSSs highlighted as colored circles (see Figure 7). The dashed lines are evolutionary tracks extracted from the BASTI database (Pietrinferni et al. 2021) for stellar masses ranging from  $0.9$  to  $1.6 M_{\odot}$ , stepped by  $0.1 M_{\odot}$ . The red solid line is the evolutionary track at  $0.8 M_{\odot}$  reproducing the cluster MS-TO region.

ure 9. The trend is less clear here than in NGC 3201 (compare with Fig. 8 in Billi et al. 2023), and the Kolmogorov-Smirnov test detects no significant difference between the radial distributions of fast and slowly rotating BSSs. Nevertheless, we can notice that the BSSs with extremely large rotational velocities ( $v \sin(i) > 200 \text{ km s}^{-1}$ ), which are also the brightest in the surveyed sample (see Fig. 7), are all concentrated in the inner region of the cluster. As discussed in Billi et al. 2023, this can be explained by assuming that the fastest (and brightest) BSSs are also the most massive ones, and they therefore suffered the effect of mass segregation that made them sink toward the cluster center. The difference in the radial distributions observed in M55 and NGC 3201 is consistent with their different value of the  $A_{rh}^+$  parameter, which quantifies the level of dynamical evolution experienced by the host cluster (Alessandrini et al. 2016). According to Ferraro et al. 2023a (see also Lanzoni et al. 2016; Ferraro et al. 2018), M55 has a value of  $A_{rh}^+$  significantly smaller than NGC 3201 ( $A_{rh}^+ = 0.10$ , compared to 0.19). This clearly indicates that M55 is less dynamical evolved than NGC 3201, consistently with the detected difference in the trend between  $v \sin(i)$  and radial distance between the two clusters.

The comparison of the CMD position of the measured BSSs with theoretical evolutionary tracks can provide some additional insights. We should remind that caution is needed in estimating the mass of BSSs from the comparison with evolutionary tracks computed for normal single stars. However, Raso et al. 2019 found a reasonable agreement between the masses derived from single star evolutionary tracks and those estimated from the fitting of the observed spectral energy distribution, thus suggesting that the former can be used at least as first-guess indication. Figure 10 shows the CMD of M55 zoomed in the BSS region, with the dashed lines corresponding to single-mass theoretical tracks extracted from the BASTI database (Pietrinferni et al. 2021) for masses ranging from  $0.9$  to  $1.6 M_{\odot}$ , stepped by  $0.1 M_{\odot}$ . The posi-

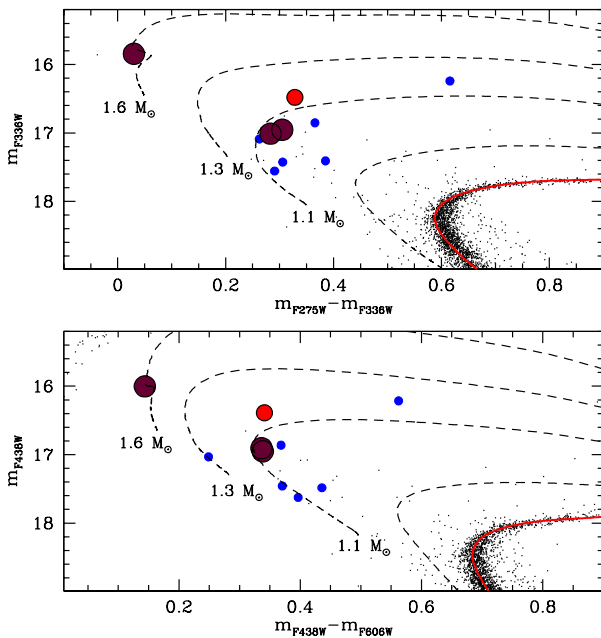


**Fig. 11.** As in Fig. 10, but for the BSSs sampled in the HST Wide Field Camera 3 (WFC3) field of view and for different color-magnitude combinations (see x- and y-labels). The four FR-BSSs are #100108 (the brightest and bluest one), #200204 and #200196 (the other large violet circles), and #200142 (red circle).

tion of the fastest rotators in the sample (i.e., the four BSSs with rotation velocity larger than  $190 \text{ km s}^{-1}$ ) suggests that 3 of them (namely #200196, #200204, #2700733) have masses of the order of  $1.1 M_{\odot}$ , and the brightest object (#100108) is as massive as  $\sim 1.5 M_{\odot}$ , very close to twice the cluster TO-mass.

This latter deserve a few comments. In fact, the Ca II K line is not visible in the spectrum of this very hot ( $T_{\text{eff}} > 9700 \text{ K}$ ) BSS, because its extremely large rotational velocity has spread out the line and made it indistinguishable from the continuum. Hence, the assumed velocity of  $200 \text{ km s}^{-1}$  is indeed a lower limit. This BSS is located in the innermost region of the cluster, at only  $52''$  from the center, where optical, ground-based observations could be problematic. To confirm its peculiar position in the CMD, we therefore used HST data acquired with the WFC3 in the context of the HST UV Legacy Survey of Galactic GCs (see Piotto et al. 2015; Nardiello et al. 2018). Figure 11 shows the CMD of M55 obtained in different HST filter combinations, with the BSSs included in the WFC3 field of view highlighted as large colored circles (same symbols as in Fig. 10). Clearly, star #100108 is the bluest and the brightest BSS, with a position well compatible with a mass of the order of  $1.5 - 1.6 M_{\odot}$ , in all filter combinations.

The evolutionary time of such a relatively massive star is expected to be quite fast, thus indicating that the formation of this BSS must have occurred recently. Interestingly, the evolutionary time read along the stellar track indicates that a  $1.5 M_{\odot}$  star needs approximately 1 Gyr to reach the current CMD position of star #100108, from the instant of formation. Thus, this seems to be a BSS that, 1 Gyr after its formation, is spinning at a velocity larger than  $200 \text{ km s}^{-1}$ . Following this line of reasoning, the other three very FR-BSSs, which have masses significantly smaller ( $\sim 1.1 M_{\odot}$ ) than BSS #100108, should be still spinning very rapidly after 3 Gyr from their formation. The reading of the evolutionary time from single star theoretical tracks therefore

suggests a not particularly efficient braking mechanism, with newly-formed BSSs being able to maintain a strong rotation for a few Gyrs. However, we notice that also the FR-BSS #2700834 (which is classified as a contact binary with ongoing MT activity; see Kaluzny et al. 2010) is located at the same position in the CMD (see Fig. 7). This suggests that 1-3 Gyr old BSSs, and BSSs on the way of their formation can occupy the same region of the diagram during their evolution, as it is indeed predicted by theoretical MT models specifically designed to describe the BSS population of M30 (see Xin et al. 2015; Jiang et al. 2017). Thus, while a first-guess estimate of BSS masses can be reasonably derived from the comparison with single star evolutionary tracks, extreme caution must be taken in reading the evolutionary time-scale from the same models. This emphasizes the urgency of complete grids of MT-BSS models for an appropriate reading of the BSS evolutionary path.

*Acknowledgements.* This work is part of the project *Cosmic-Lab* (Globular Clusters as Cosmic Laboratories) at the Physics and Astronomy Department “A. Righi” of the Bologna University (<http://www.cosmic-lab.eu/Cosmic-Lab/Home.html>). A.B. acknowledges funding from the European Union NextGenerationEU.

## References

Alessandrini, E., Lanzoni, B., Ferraro, F. R., Miocchi, P., & Vesperini, E. 2016, ApJ, 833, 252  
 Andronov, N., Pinsonneault, M. H., & Terndrup, D. M. 2006, ApJ, 646, 1160  
 Baumgardt, H., & Hilker, M. 2018, MNRAS, 478, 1520  
 Beccari, G., Ferraro, F. R., Dalessandro, E., et al. 2019, ApJ, 876, 87  
 Behr, B. B., Cohen, J. G., & McCarthy, J. K. 2000a, ApJ, 531, L37  
 Behr, B. B., Djorgovski, S. G., Cohen, J. G., et al. 2000b, ApJ, 528, 849  
 Benz, W., & Hills, J. G. 1987, ApJ, 323, 614  
 Billi, A., Ferraro, F. R., Mucciarelli, A., et al. 2023, ApJ, 956, 124  
 Cadelano, M., Ferraro, F. R., Dalessandro, E., et al. 2022, ApJ, 941, 69  
 Castelli, F., Gratton, R. G., & Kurucz, R. L. 1997, A&A, 318, 841  
 Castelli, F., & Kurucz, R. L. 2003, in Modelling of Stellar Atmospheres, ed. N. Piskunov, W. W. Weiss, & D. F. Gray, Vol. 210, A20  
 Dalessandro, E., Ferraro, F. R., Massari, D., et al. 2013, ApJ, 778, 135  
 Davies, M. B., Piotto, G., & de Angeli, F. 2004, MNRAS, 349, 129  
 De Marco, O., Shara, M. M., Zurek, D., et al. 2005, ApJ, 632, 894  
 de Mink, S. E., Langer, N., Izzard, R. G., Sana, H., & de Koter, A. 2013, ApJ, 764, 166  
 Ferraro, F. R., Beccari, G., Dalessandro, E., et al. 2009, Nature, 462, 1028  
 Ferraro, F. R., Carretta, E., Corsi, C. E., et al. 1997, A&A, 320, 757  
 Ferraro, F. R., D’Amico, N., Possenti, A., Mignani, R. P., & Paltrinieri, B. 2001, ApJ, 561, 337  
 Ferraro, F. R., Fusi Pecci, F., & Bellazzini, M. 1995, A&A, 294, 80  
 Ferraro, F. R., Fusi Pecci, F., & Buonanno, R. 1992, MNRAS, 256, 376  
 Ferraro, F. R., Lanzoni, B., & Dalessandro, E. 2020, Rendiconti Lincei. Scienze Fisiche e Naturali, 31, 19  
 Ferraro, F. R., Lanzoni, B., Dalessandro, E., et al. 2012, Nature, 492, 393  
 Ferraro, F. R., Lanzoni, B., Dalessandro, E., et al. 2019, Nature Astronomy, 3, 1149  
 Ferraro, F. R., Lanzoni, B., Raso, S., et al. 2018, ApJ, 860, 36  
 Ferraro, F. R., Lanzoni, B., Vesperini, E., et al. 2023a, ApJ, 950, 145  
 Ferraro, F. R., Mucciarelli, A., Lanzoni, B., et al. 2023b, Nature Communications, 14, 2584  
 Ferraro, F. R., Pecci, F. F., Cacciari, C., et al. 1993, AJ, 106, 2324  
 Ferraro, F. R., Sabbi, E., Gratton, R., et al. 2006, ApJ, 647, L53  
 Ferraro, F. R., Sills, A., Rood, R. T., Paltrinieri, B., & Buonanno, R. 2003, ApJ, 588, 464  
 Fiorentino, G., Lanzoni, B., Dalessandro, E., et al. 2014, ApJ, 783, 34  
 Geller, A. M. & Mathieu, R. D. 2011, Nature, 478, 356  
 Gilliland, R. L., Bono, G., Edmonds, P. D., et al. 1998, ApJ, 507, 818  
 Gosnell, N. M., Mathieu, R. D., Geller, A. M., et al. 2014, ApJ, 783, L8  
 Gosnell, N. M., Mathieu, R. D., Geller, A. M., et al. 2015, ApJ, 814, 163  
 Harris, W. E. 1996, AJ, 112, 1487  
 Hills, J. G. & Day, C. A. 1976, Astrophys. Lett., 17, 87  
 Jiang, D., Chen, X., Li, L., & Han, Z. 2017, ApJ, 849, 100  
 Kaluzny, J., Thompson, I. B., Krzeminski, W., & Zloczewski, K. 2010, Acta Astron., 60, 245  
 Kurucz, R. 1993, ATLAS9 Stellar Atmosphere Programs and 2 km/s grid. Kurucz CD-ROM No. 13. Cambridge, 13

Kurucz, R. L. 2005, Memorie della Societa Astronomica Italiana Supplementi, 8, 14

Lanzoni, B., Dalessandro, E., Perina, S., et al. 2007, ApJ, 670, 1065

Lanzoni, B., Ferraro, F. R., Alessandrini, E., et al. 2016, ApJ, 833, L29

Leigh, N., Knigge, C., Sills, A., et al. 2013, MNRAS, 428, 897

Leigh, N., Sills, A., & Knigge, C. 2007, ApJ, 661, 210

Leiner, E., Mathieu, R. D., Gosnell, N. M., & Sills, A. 2018, ApJ, 869, L29

Leonard, P. J. T. & Livio, M. 1995, ApJ, 447, L121

Lombardi, J. C. J., Rasio, F. A., & Shapiro, S. L. 1995, ApJ, 445, L117

Lovisi, L., Mucciarelli, A., Dalessandro, E., Ferraro, F. R., & Lanzoni, B. 2013a, ApJ, 778, 64

Lovisi, L., Mucciarelli, A., Ferraro, F. R., et al. 2010, ApJ, 719, L121

Lovisi, L., Mucciarelli, A., Lanzoni, B., et al. 2013b, ApJ, 772, 148

Lovisi, L., Mucciarelli, A., Lanzoni, B., et al. 2012, ApJ, 754, 91

Mathieu, R. D. & Geller, A. M. 2009, Nature, 462, 1032

McCrea, W. H. 1964, MNRAS, 128, 147

Milliman, K. E., Mathieu, R. D., & Schuler, S. C. 2015, AJ, 150, 84

Mucciarelli, A., Lovisi, L., Ferraro, F. R., et al. 2014, ApJ, 797, 43

Nardiello, D., Libralato, M., Piotto, G., et al. 2018, MNRAS, 481, 3382

Nine, A. C., Mathieu, R. D., Schuler, S. C., & Milliman, K. E. 2024, ApJ, 970, 187

Packet, W. 1981, A&A, 102, 17

Pasquini, L., Avila, G., Blecha, A., et al. 2002, The Messenger, 110, 1

Perets, H. B. & Fabrycky, D. C. 2009, ApJ, 697, 1048

Pietrinferni, A., Hidalgo, S., Cassisi, S., et al. 2021, ApJ, 908, 102

Piotto, G., De Angeli, F., King, I. R., et al. 2004, ApJ, 604, L109

Piotto, G., Milone, A. P., Bedin, L. R., et al. 2015, AJ, 149, 91

Portegies Zwart, S. 2019, A&A, 621, L10

Raso, S., Pallanca, C., Ferraro, F. R., et al. 2019, ApJ, 879, 56

Sarna, M. J. & De Greve, J. P. 1996, QJRAS, 37, 11

Sbordone, L., Bonifacio, P., Castelli, F., & Kurucz, R. L. 2004, Memorie della Societa Astronomica Italiana Supplementi, 5, 93

Shara, M. M., Saffer, R. A., & Livio, M. 1997, ApJ, 489, L59

Sills, A., Adams, T., & Davies, M. B. 2005, MNRAS, 358, 716

Sills, A., Adams, T., Davies, M. B., & Bate, M. R. 2002, MNRAS, 332, 49

Sills, A. & Pinsonneault, M. H. 2000, ApJ, 540, 489

Sollima, A., Lanzoni, B., Beccari, G., Ferraro, F. R., & Fusi Pecci, F. 2008, A&A, 481, 701

Stetson, P. B., Pancino, E., Zocchi, A., Sanna, N., & Monelli, M. 2019, MNRAS, 485, 3042

Sun, M., Gossage, S., Leiner, E. M., & Geller, A. M. 2024, arXiv e-prints, arXiv:2403.17279

Tonry, J. & Davis, M. 1979, AJ, 84, 1511

VandenBerg, D. A., Brogaard, K., Leaman, R., & Casagrande, L. 2013, ApJ, 775, 134

Vink, J. S. & Cassisi, S. 2002, A&A, 392, 553

Xin, Y., Ferraro, F. R., Lu, P., et al. 2015, ApJ, 801, 67